

Journal of Geophysical Research: Oceans**RESEARCH ARTICLE**

10.1002/2014JC009960

Special Section:

Early scientific results from the salinity measuring satellites Aquarius/SAC-D and SMOS

Key Points:

- SMOS provides a successful opportunity to observe SSS signals of TIWs from space
- The westward propagations of SSS and SST signals appeared seasonally
- Westward propagation speed of SMOS SSS signals ranges between 0.6 and 1.5 m/s

Supporting Information:

- Readme
- TIW_animation.swf
- SSS_SST_animation.swf

Correspondence to:

X. Yin,
xylod@locean-ipsl.upmc.fr

Citation:

Yin, X., J. Boutin, G. Reverdin, T. Lee, S. Arnault, and N. Martin (2014), SMOS Sea Surface Salinity signals of tropical instability waves, *J. Geophys. Res. Oceans*, 119, 7811–7826, doi:10.1002/2014JC009960.

Received 20 MAR 2014

Accepted 13 OCT 2014

Accepted article online 17 OCT 2014

Published online 20 NOV 2014

SMOS Sea Surface Salinity signals of tropical instability waves

Xiaobin Yin^{1,2}, Jacqueline Boutin², Gilles Reverdin², Tong Lee³, Sabine Arnault², and Nicolas Martin²

¹ARGANS, Plymouth, UK, ²Sorbonne Universités (UPMC, Université Paris 06), CNRS, IRD, MNHN, LOCEAN Laboratory, Paris, France, ³Jet Propulsion Laboratory, California Institute of Technology, Pasadena, California, USA

Abstract Sea Surface Salinity (SSS) measurements from the Soil Moisture and Ocean Salinity (SMOS) mission provide an unprecedented opportunity to observe the salinity structure of tropical instability waves (TIWs) from space, especially during the intense 2010 La Niña condition. In the eastern equatorial Pacific Ocean, SMOS SSS signals correlate well and have similar amplitude to 1 m salinity from the Tropical Atmosphere Ocean (TAO) array at six locations with strong TIW signals. At these locations, the linear negative relationships between SMOS SSS and OSTIA SST signals vary from $-0.20^{\circ}\text{C}^{-1}$ to $-0.25^{\circ}\text{C}^{-1}$, which are comparable to the ones obtained from TAO. From June to December 2010, the largest TIW signals and meridional gradients of both SSS and SST appear around 2°N west of 100°W . They shift southward and cross the equator at 90°W . In addition to the large negative correlation band around 2°N , a band of negative correlations between SSS and SST signals also exists around 8°N west of 110°W for the 33 day signals. The peak amplitude of the 33 day SMOS SSS signals west of 135°W is reduced by >40% with respect to values east of 135°W , while the reduction for SST is much lower (<20%). The amplitudes and longitudinal extents of TIW signals and the dominant westward propagation speed of 17 day TIWs (as detected by SMOS and Aquarius) at the equator decrease from 2010 to 2013 associated with the transition from a strong La Niña to non-La Niña conditions.

1. Introduction

In both the Atlantic and Pacific Oceans, a tongue of cold surface water usually extends from the continental margins westward along the equator during non-El Niño conditions. This “cold tongue” consists of water upwelled from the thermocline, and is surrounded by warmer tropical surface waters on both sides of the equator. Tropical instability waves (TIWs) are a phenomenon in which the interface between areas of warm and cold Sea Surface Temperatures (SST) near the equator forms a regular pattern of westward propagating waves [Legeckis and Reverdin, 1987; Chelton et al., 2000]. They are caused by barotropic and baroclinic instability associated with the meridional and vertical shear between the westward-flowing South Equatorial Current and the eastward flowing Equatorial Undercurrent and Equatorial Counter-current [Masina et al., 1999; Grodsky et al., 2005; Willett et al., 2006]. The shear at the northern edge of the cold tongues is stronger than at the southern edge [Jochum and Murtugudde, 2006], resulting in stronger TIWs in the north. TIW amplitudes have a largest amplitude between June and November [Polito et al., 2001; Liu et al., 2000]. They are also larger during La Niña conditions when the cold tongue and the related current shear are more intense than those during a normal year. TIWs are found to play important roles in mixing and cross-equator transport of sea water [Jochum and Murtugudde, 2006; Menkes et al., 2006], the modulation of the heat budget of the ocean mixed layer [Swenson and Hansen, 1999; Vialard et al., 2003], air-sea coupling [Liu et al., 2000; Yu and Liu, 2003], and marine biogeochemistry [Boutin et al., 1999; Gorgues et al., 2005; Evans et al., 2009].

TIWs generally fall into two categories. The first one has periods around 15–23 days, is most prominent in meridional current velocity, and has been observed within a few degrees of the equator [Qiao and Weisberg, 1995; Kennan and Flament, 2000; Lyman et al., 2007]. The second one has periods around 1 month and has been observed in sea surface height, thermocline depth, velocity, and subsurface temperature centered about 5°N [Kennan and Flament, 2000; Lyman et al., 2007; Shinoda et al., 2009]. The dominant phase speeds of TIWs range between 0.3 and 1.0 m/s in the Pacific Ocean [Qiao and Weisberg, 1995; Chelton et al., 2000]. TIWs have been detected in the atmospheric boundary layer and modulations of ocean surface wind stress as observed by scatterometers [Liu et al., 2000; Polito et al., 2001; Yu and Liu, 2003]. The TIW pattern is also identifiable in chlorophyll *a* (chl *a*) [Strutton et al., 2001; McClain et al., 2002; Lee et al., 2012].

Most of these earlier analyses disregarded salinity. Grodsky *et al.* [2005] have analyzed mooring data in the tropical Atlantic Ocean and shown that TIW induced temperature variations are accompanied by out-of-phase salinity variations. The spatial and temporal variabilities of ocean surface salinity in the tropical eastern and central Pacific Ocean are poorly known mostly because in situ salinity observations are sparse. With the advent of satellite salinity measurements, it is now possible to analyze the salinity signal associated with TIWs [Lee *et al.*, 2012]. This provides a significant new capability to the scope of TIW observations that has important implications to ocean circulation and climate [Lagerloef, 2008]. Lee *et al.* [2012] have studied the TIWs from September to December 2012 using Aquarius Sea Surface Salinity (SSS). Major results in that study are: (1) Different from SST and sea surface height anomaly, where the largest signals of TIWs are found a few degrees north of the equator, the SSS signature of TIWs is strongest near the equator. (2) The magnitude of SSS anomaly associated with TIWs is approximately 0.5 (larger in the east and smaller in the west). (3) The 17 day TIWs at the equator have a 1 m/s dominant phase speed and the 33 day TIWs have a 0.5 m/s dominant phase speed. Due to the limited period of that study, it could not look at interannual variations of TIWs. This is one of the topics to be addressed by the present study.

The European Soil Moisture and Ocean Salinity (SMOS) satellite, launched in November 2009, has been providing global monitoring of SSS since January 2010. It offers an unprecedented opportunity to study the salinity signal and propagation associated with TIWs during recent years. SMOS and Aquarius missions monitor SSS in different ways. Aquarius is a combined active/pассив L-band microwave instrument [Yueh *et al.*, 2013], whereas SMOS is an interferometric L-band microwave radiometer. Although TIWs have been studied using Aquarius SSS [Lee *et al.*, 2012], the capability of monitoring TIWs from SMOS is not known a priori even though SMOS characteristics suggest good feasibility (e.g., 43×43 km spatial resolution, 1200 km swath and 3 day revisit sampling). Also, the SMOS mission offers an unprecedented opportunity to monitor the intense 2010 La Niña condition which was missed by the Aquarius mission launched 1 year later in June 2011. Furthermore, how well SMOS detects TIWs, especially in comparison with TAO mooring data, needs to be documented and demonstrated. Here we use SMOS data to provide an analysis of space-borne SSS signal associated with TIWs in the tropical Pacific Ocean, aided by a characterization of TIWs using satellite-derived SST. To complement the previous studies, we also investigate the correlation between space-borne measurements of SSS and SST in terms of phase and magnitude. Data and methods are described in section 2, results are presented in section 3, and summarized and discussed in section 4.

2. Data Description and Methods

SMOS level 3 SSS maps (combined ascending and descending orbits) averaged with 10 day, 100×100 km² running windows and sampled daily over a $0.25^\circ \times 0.25^\circ$ grid have been generated at Laboratoire d'Océanographie et du Climat: Expérimentation et Approches Numériques (LOCEAN) (<http://catds.ifremer.fr/Products/Available-products-from-CEC-OS/Locean-v2013>) [Boutin *et al.*, 2013; Yin *et al.*, 2012a]. These products are built from ESA level 2 SSS. Contrary to the Centre Aval de Traitement des Données SMOS (CATDS) Expertise Centers (CEC) Institut français de recherche pour l'exploitation de la mer (IFREMER) products [Reul and Tenerelli, 2011], they do not contain any relaxation to climatology which may reduce the TIW signature. Indeed, tests performed with CATDS CEC-IFREMER products show peak-to-peak amplitudes of SSS TIW signals much lower than the ones shown in this paper. SMOS SSS is not used before June 2010 due to the variable configurations for testing the functionalities of the instrument and low-level procedures for data acquisition and handling during In-Orbit Commissioning Phase [Corbella *et al.*, 2011].

We also use daily SST from the Operational Sea Surface Temperature and Sea Ice Analysis (OSTIA) produced on an operational basis at the UK Met Office using optimal interpolation on a global 0.054° grid [Donlon *et al.*, 2012]. The SST maps were resampled over the same 0.25×0.25 grid as the SSS maps.

Near 5°N , the SMOS SSS vortices associated with TIWs are well observed together with clockwise rotating patterns of currents taken from Ocean Surface Current Analyses-Real time (OSCAR) [Bonjean and Lagerloef, 2002] (Figure 1a). The combined action of sets of tropical instability vortices (TIVs) is likely to generate the cusp-shaped TIW patterns both in the SMOS SSS and the OSTIA SST (Figures 1a and 1b). The SSS cusps are particularly noticeable in the northern hemisphere, with the northward higher SSS cusps coinciding with that of the lower SST (supporting information SSS_SST_animation.swf).

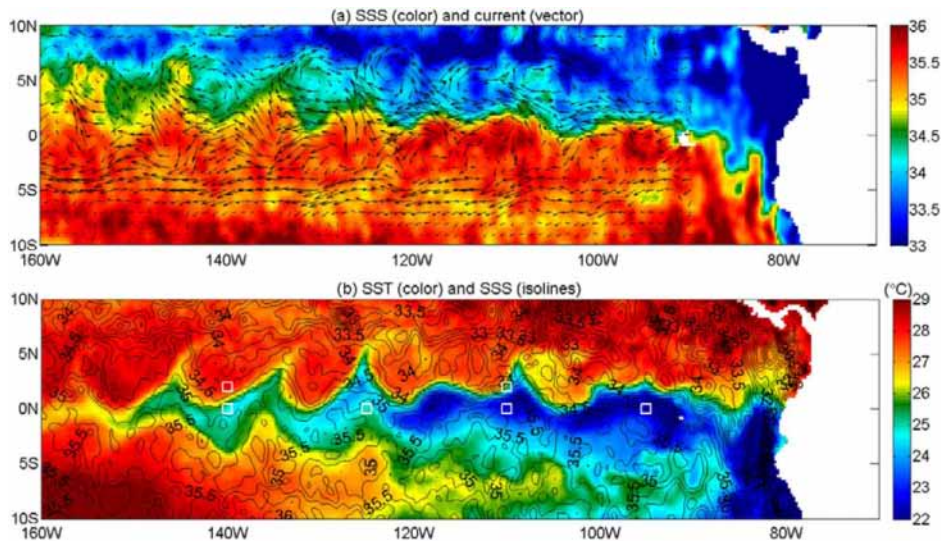


Figure 1. (a) 10 day average SMOS SSS (color shading) and 5 day average OSCAR currents (vectors), and (b) daily OSTIA SST (color shading) and 10 day average SMOS SSS (isolines) centered on 24 September 2010. The white squares in Figure 1b correspond to the TAO moorings used for comparisons of SSS and SST.

As the periods generally associated with TIWs are <50 days, SSS and SST signals with periods longer than 50 days, in particular the seasonal variability, are removed by 50 day high-pass (50d-HP) filtering. Then SSS and SST signals associated with TIWs are isolated using both 28–40 day band-pass filtering (referred to as 33 day) and 13–22 day band-pass (17 day) filtering, corresponding to 33 and 17 day periods, respectively. The results are robust and remain unchanged when we slightly alter the period bands (as, for example, 45 or 55 day high-pass, and 25–40 day or 10–25 day band pass).

Data from the Tropical Atmosphere Ocean (TAO) mooring array are also used in this analysis. They include SSS and SST daily data at 1 m depth from June to December 2010. TAO SSS and SST are filtered using the same high-pass filtering and band-pass filtering as previously described. Filtered TAO data are then compared with SMOS SSS and OSTIA SST signals associated with TIWs. Six moorings, with time series longer than 100 days from June to December 2010 and with peak amplitude of 33 day SSS signals larger than 0.1, are selected for comparisons (Table 1). Only high quality flagged (flag = 1) TAO SSS and SST [Henocq et al., 2010] are used for analysis. Dubious TAO SSS at 140°W, 2°N from mid-September to December 2010 are also removed. At 140°W, 0°N, we observe a systematic positive bias between TAO SSS at 1 and 20 m depth, which increases from 0.2 in early June to 0.4 in late September, and then becomes roughly stationary till late November and disappears on 27 November when the mooring has been replaced. The Array for Real-Time Geostrophic Oceanography (ARGO) SSS measured at 5 m depth collocated with a radius of 50 km and ± 5 days with the mooring are consistent with TAO SSS at 20 m depth. After 27 November, TAO SSS at 1 and 20 m depths and ARGO SSS are very consistent. Hence, before 27 November, we have adjusted the

Table 1. Correlation Coefficients r Between Filtered SMOS SSS and TAO SSS (the 95% Significant Values are Indicated in Bold Italics), Peak Amplitude of SMOS SSS Signals and STD Ratios of SMOS SSS Signals to That of TAO SSS Signals^a

Mooring	Number of SSS	33 Day Band Pass			17 Day Band Pass		
		r	Amplitude	STD Ratio	r	Amplitude	STD Ratio
95W, 0N	136	0.98	0.31	1.43	0.90	0.49	1.21
110W, 2N	131	0.97	0.32	1.78	0.67	0.45	1.38
110W, 0N	141	0.98	0.25	2.58	0.91	0.28	1.32
125W, 0N	199	0.93	0.27	1.41	0.78	0.26	1.40
140W, 2N	107	0.93	0.15	0.86	0.75	0.11	1.02
140W, 0N (adjusted)	196	0.38	0.20	1.32	0.86	0.15	0.93

^aOnly moorings with time series longer than 100 days from June to December 2010 and with peak amplitude of SSS 33 day signals larger than 0.1 are selected.

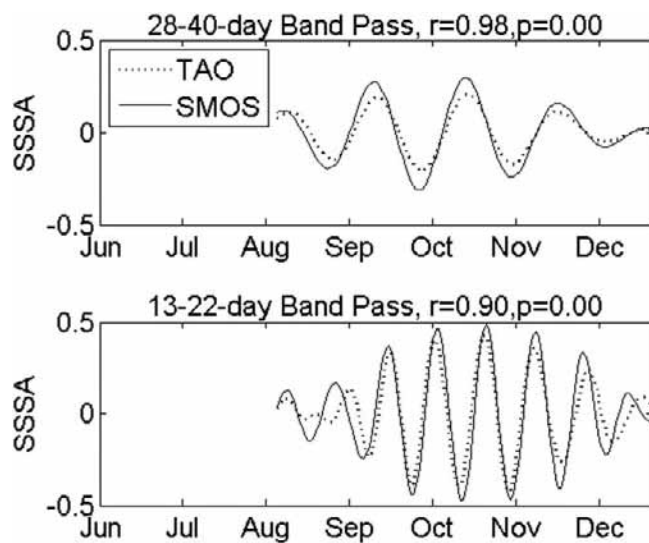


Figure 2. TAO SSS (dots) and SMOS SSS (lines) at 95°W, 0°N for the (top) 33 day and (bottom) 17 day filtered series from June to December 2010. Correlation coefficients r between the TAO and SMOS SSS and p values for testing the hypothesis of no correlation are given in the title of each plot. Only p values <0.05 correspond to a significant correlation.

ment is quite good at 95°W, 0°N for both period bands. Table 1 reports the correlation coefficients between the SMOS and TAO SSS filtered signals, together with the peak amplitudes of SMOS SSS filtered signals and the ratios of the standard deviation (STD) of SMOS versus TAO SSS filtered signals, for the equatorial mooring presented in Figure 2 and for five other mooring locations within the region of 110°W–140°W, 2°N–0°N (squares in Figure 1b). SMOS level 3 SSS maps are averaged with a 10 day running window, the time span of which is close to 17 day. The SMOS 17 day signal is therefore expected to be more influenced by this tie averaging than the 33 day signal. Hence, only moorings with time series longer than 100 days from June to December 2010 and with peak amplitude of SSS 33 day signals larger than 0.1 are selected. The correlation coefficients for the 33 day filtered series are higher, exceeding 0.90 except for the mooring at 140°W, 0°N that was bias corrected (without bias correction the correlation coefficient was –0.27) (Table 1). The STD ratios depend on the location. However, apart from the TAO mooring at 140°W, 2°N, the ratios are all above 1, indicating a stronger variability for SMOS SSS than for TAO SSS for this period band. The highest SSS STD ratio of 2.58 is found at 110°W, 0°N (Table 1) whereas the ratio of the STD of OSTIA to TAO SST filtered signals is also high, being 2.20 (Table 2). For the 33 day signals, the variability in OSTIA SST is stronger than in TAO SST (i.e., STD ratio above 1) for all six moorings (Table 2). For the 17 day SSS filtered signal, the correlations vary from 0.67 to 0.91. The STD ratios ranging from 0.93 to 1.40 indicate a rather similar variability shown by SMOS and TAO, except again at the westernmost location 140°W, 0°N where the SMOS variability is lower than that of the TAO SSS. However, STD ratios of OSTIA versus TAO SST filtered signals are also lower than 1 at the two moorings located at 95°W, 0°N and 140°W, 0°N (Table 2). SMOS SSS estimates SSS in the top centimeter of the ocean and OSTIA merges satellite SST from different sensors which skin depths

TAO SSS at 1 m depth to TAO SSS at 20 m depth, considering days with no SST stratification to estimate the biases and assuming that the biases evolve linearly in time.

The 7 day maps of version 2.0, level 3, Aquarius SSS data based on the Combined Active Passive (CAP) retrieval algorithm [Yueh et al., 2013] are used for the comparison between SMOS and Aquarius SSS from September 2011 to June 2013.

3. Results

3.1. Comparison Between SMOS and TAO Filtered Signals

Figure 2 shows a comparison between SMOS and TAO SSS filtered signals at 95°W, 0°N from June to December 2010. The agree-

Table 2. Correlation Coefficients r Between Filtered OSTIA SST and TAO SST (the 95% Significant Values are Indicated in Bold Italics), Peak Amplitude of OSTIA SST Signals and STD Ratios of OSTIA SST Signals to that of TAO SST Signals^a

Mooring	Number of SST	33 Day Band Pass			17 Day Band Pass		
		r	Amplitude (°C)	STD Ratio	r	Amplitude (°C)	STD Ratio
95W, 0N	136	0.99	1.05	1.02	0.91	2.05	0.97
110W, 2N	131	0.89	0.63	1.61	0.98	1.90	1.06
110W, 0N	141	0.93	0.85	2.20	0.95	1.13	1.21
125W, 0N	199	0.97	0.76	1.78	0.90	1.03	1.37
140W, 2N	107	0.99	1.08	1.14	0.94	0.63	1.02
140W, 0N	196	0.98	0.50	1.03	0.97	0.68	0.91

^aThe same moorings as Table 1 are used.

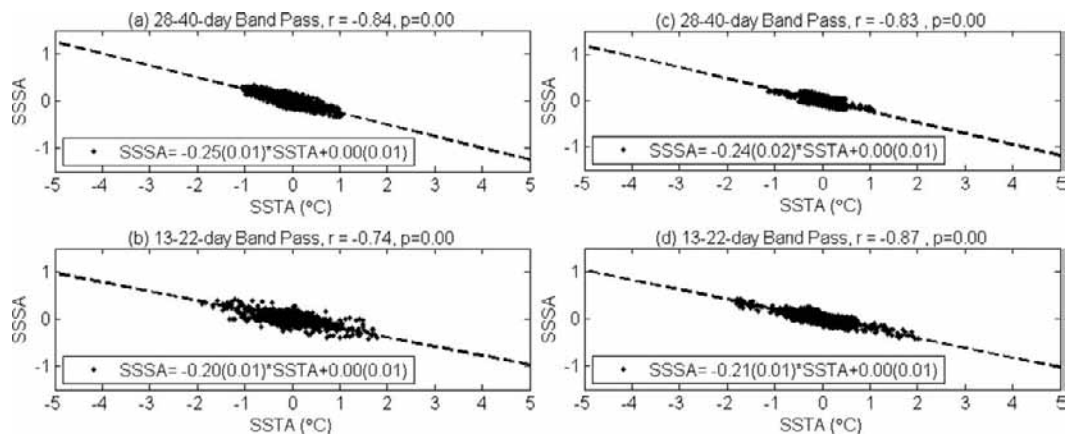


Figure 3. SMOS SSS signals versus OSTIA SST signals for (a) 33 day and (b) 17 day from June to December 2010; TAO SSS signals versus SST signals for (c) 33 day and (d) 17 day for six moorings (Table 1) during the same period. 95% confidence intervals for the coefficient estimates are given in brackets. SMOS SSS and OSTIA at positions of six TAO moorings are used. Correlation coefficients r between SSS and SST and p values for testing the hypothesis of no correlation are given in the title of each plot. Only p values <0.05 correspond to significant r .

vary from hundreds of microns to few tenths of centimeters and in situ temperature from drifting and moored buoys at different depths, whereas TAO data are measured at 1 m depth. So, differences between SMOS SSS and TAO SSS and between OSTIA SST and TAO SST may be partly due to vertical dynamics of the upper-ocean, air-sea flux, and data sampling.

In the following, we examine the SSS-SST relation depicted by the satellite data (SMOS and OSTIA) and by the TAO data by combining the data from the six mooring locations discussed previously (Table 1) from June to December 2010. Scatterplots of SSS versus SST filtered signals are presented for the different filters both for the satellite data and the TAO data (Figure 3). A linear relationship is seen in all scatter plots. For the 33 day period, the regression slope of the satellite data is $-0.25 (\pm 0.01) \text{ }^{\circ}\text{C}^{-1}$ whereas it is $-0.24 (\pm 0.02) \text{ }^{\circ}\text{C}^{-1}$ for the TAO moorings; for the 17 day period, the values are $-0.20 (\pm 0.01) \text{ }^{\circ}\text{C}^{-1}$ and $-0.21 (\pm 0.01) \text{ }^{\circ}\text{C}^{-1}$ for the satellite data and for the TAO data, respectively. Therefore, the SSS-SST relation seen from the satellite data is consistent with that found from the TAO data.

3.2. The Propagation of TIWs in 2010

In this section, we focus the analysis on the June to December 2010 period. As seen previously, during this period, the tropical Pacific was characterized by a strong La Niña, providing favorable conditions for the occurrence of TIWs.

Mean meridional gradients of SSS and SST, $\partial\bar{S}/\partial y$ and $\partial\bar{T}/\partial y$, are crucial parameters for the detection of TIWs as the meridional movements associated with TIWs displace these mean gradients. Therefore, the association of SSS (SST) TIW signal with $\partial\bar{S}/\partial y$ ($\partial\bar{T}/\partial y$) is expected. Furthermore, the mean SSS and SST gradients together are associated with a mean meridional density gradient, which is the source, both of potential energy for baroclinic instabilities and of the strong shears that can cause barotropic instability [Masina et al., 1999; Grodsky et al., 2005; Willett et al., 2006]. In the Pacific, strong negative $\partial\bar{S}/\partial y$ and positive $\partial\bar{T}/\partial y$ north of the equator (Figures 4a and 4b) are associated with the SSS and SST fronts in the opposite direction that bracket the equatorial salty-cold tongue (Figure 1b). East of 100°W , the northern maximum meridional gradients of SSS and SST shift southward, crossing the equator at 90°W (Figures 4a and 4b). Meridional gradients of SSS and SST reduce sharply between 115°W and 135°W (Figure 4c).

Figures 5a–5d present the STDs for filtered SSS and SST for the two different period bands. Areas with large amplitudes of SSS and SST STDs (Figures 5a–5d) generally coincide with areas of large $\partial\bar{S}/\partial y$ and $\partial\bar{T}/\partial y$ (Figures 4a and 4b). The largest filtered SSS and SST signals appear around 2°N west of 100°W . They shift southward and cross the equator at 90°W following the northern SSS and SST meridional gradients all the way to the eastern boundary. These STDs associated with TIWs are stronger to the north of the equatorial cold tongues in the Pacific in association with stronger shear in the northern edge of the cold tongues [Jochum and Murtugudde, 2006].

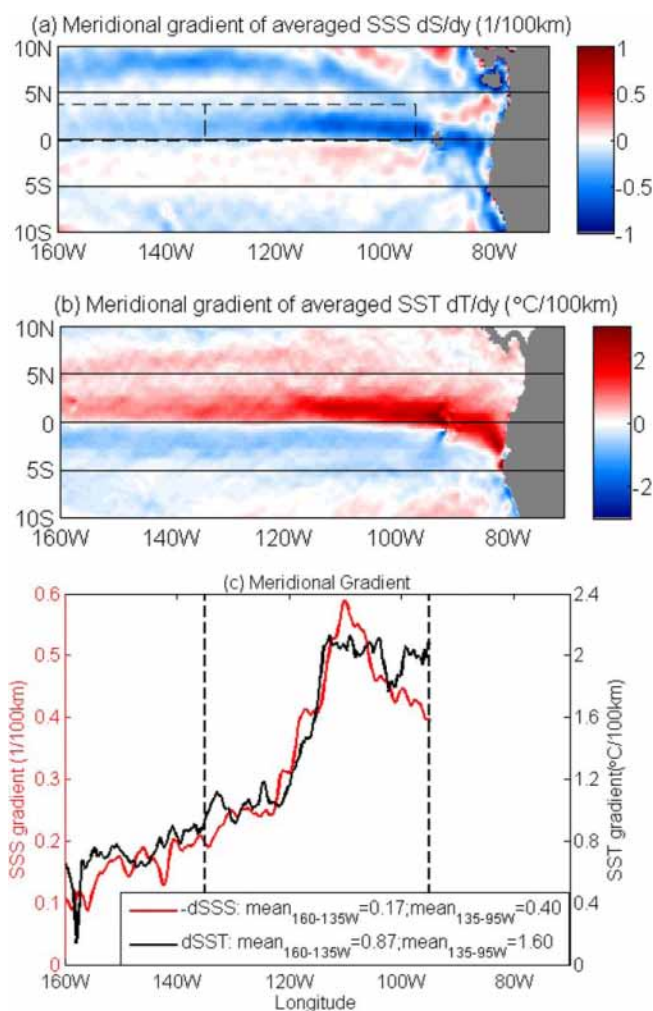


Figure 4. The meridional gradients of (a) average SMOS SSS and (b) average OSTIA SST from June to December 2010 and (c) their gradients at 2°N versus longitude. Two dashed boxes ([0°N–4°N, 95°W–135°W] and [0°N–4°N, 135°W–160°W]) shown in Figure 4a are used for statistics in Table 3. Mean meridional gradients between 135°W and 160°W and between 135°W and 95°W at 2°N are listed in Figure 4c. Vertical dash lines in Figure 4c correspond to 135°W and 95°W.

west of 110°W for the 33 day signals (Figure 7a). The correlations in the region near 5°N between the two high-correlation bands are low (Figure 7a). Though the cusp-like shapes of low SST and high SSS are clearly observed near 8°N, it is more complicated with TIV cores centering near 5°N (Figure 1). TIVs have a complex three-dimensional circulation from the surface down to the thermocline [Kennan and Filament, 2000]. At the leading western edge of the vortex, the flow decelerates, resulting in convergence and downwelling [Menkes et al., 2002]. As the flow recirculates anticyclonically, upwelling occurs from the trailing east edge to the core of the vortex [Dutrieux et al., 2008]. Thus the simple correlation of cold SST and salty SSS associated with TIWs breaks down near this latitude.

On the longitude-time Hovmöller diagrams along 2°N of the various filtered SSS and SST signals (Figure 8), westward propagations are evident. However, these propagations are generally more pronounced and extend further west on SST than on SSS. The peak amplitude of the 33 day SMOS SSS signals west of 135°W is reduced by >40% with respect to values east of 135°W (Figure 5e), while the reduction is <20% for SST (Figure 5e). This indicates that the east-west contrasts of peak amplitudes of the 33 day SMOS SSS signals are stronger than in OSTIA SST filtered signals. This is likely due to the stronger east-west contrasts for the SSS meridional gradients than for the SST meridional gradients (Figure 4c). However, the east-west contrasts of peak amplitudes of the 17 day filtered SMOS SSS signals are similar to the 17 day filtered OSTIA SST

SSS and SST filtered signals vary approximately out-of-phase (supporting information TIW_animation.swf). To further illustrate this out-of-phase relation, we show time series of the daily signals of SSS and SST at 120°W, 2°N using the three filters in Figure 6. The correlation coefficients between these SSS and SST filtered signals from June to December 2010 are displayed in Figure 7 over the eastern Pacific domain. An equatorially trapped band of negative correlations between SSS and SST signals appears just north of the equator west of 100°W and moves southward further east to cross the equator at 90°W. These patterns follow the SSS and SST meridional gradients (Figures 4a and 4b). The correlation of the 33 day SSS and SST signals is stronger than the 17 day ones.

The negative correlation coefficients between SMOS SSS and OSTIA SST indicate coherent physical processes that regulate the two variables. Advection of the equatorial upwelling plume by horizontal flows and related fluctuations in upwelling, vertical mixing, and entrainment can lead to opposite signals in SSS and SST. However, the discussion of SSS variations due to the vertical TIW-induced velocity is out of scope of this paper.

In addition to the equatorial large correlation band, a band of negative correlations also exists around 8°N

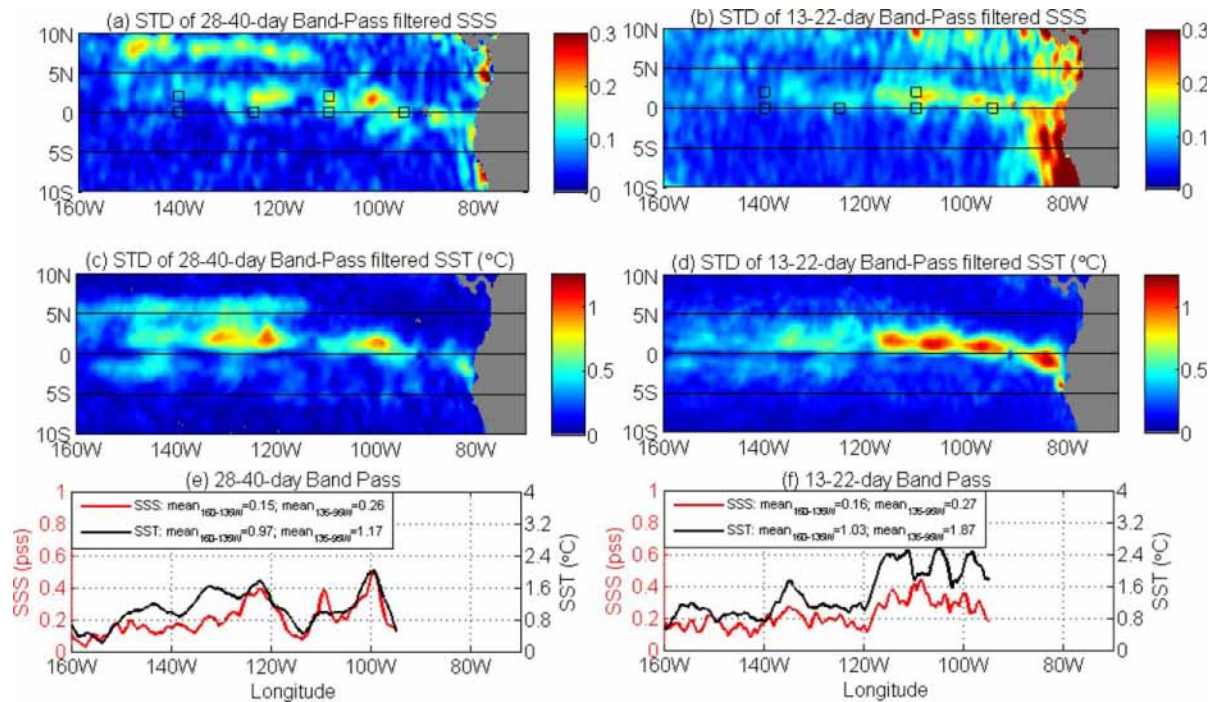


Figure 5. (a, c) STD of SMOS SSS and (b, d) OSTIA SST filtered signals from June to December 2010, and (e, f) peak amplitudes of the filtered signals at 2°N versus longitude for the same period. Figures 5a, 5c, and 5e correspond to 33 day filtered signals and Figures 5b, 5d, and 5f correspond to 17 day filtered signals. The squares in Figures 5a and 5c correspond to the TAO moorings used for comparisons of SSS and SST. Mean peak amplitudes between 135°W and 160°W and between 135°W and 95°W at 2°N are listed in Figures 5e and 5f.

signals (Figure 5f). This feature stands also for the equator (Figure 9). The linear fits of SSS and SST filtered signals and their correlation coefficients from June to December 2010, in the two rectangular regions east and west of 135°W shown in Figure 4a, are listed in Table 3. The magnitude of the fits and the correlation coefficients in the eastern box are higher than the values in the western boxes, partially due to the differences between the east-west contrast of peak amplitudes of SMOS SSS and OSTIA SST filtered signals.

The 33 day TIWs are dominant between 160°W and 110°W at 2°N. This can be seen in Figures 8a and 8c. A Radon transform estimate of the phase speed [Challenor *et al.*, 2001] gives a dominant westward propagation of 0.6 m/s for these 33 day signals west of 110°W. This value is a widely reported one for TIW phase

speed [Chelton *et al.*, 2000; Polito *et al.*, 2001]. Lyman *et al.* [2007] state that 33 day TIWs are not associated with a meridional velocity signal on the equator. Figures 9a and 9c, same as Figure 8 except that the equator is selected instead of 2°N, clearly show a reduced activity for these 33 day TIWs west of 110°W.

The dominant westward propagation speeds of 17 day filtered SSS and SST at 2°N are also about 0.6 m/s (Figures 8b and 8d), thus identical to the 33 day ones. These 17 and 33 day waves have almost identical phase speeds, which suggest they may arise from the same critical latitude

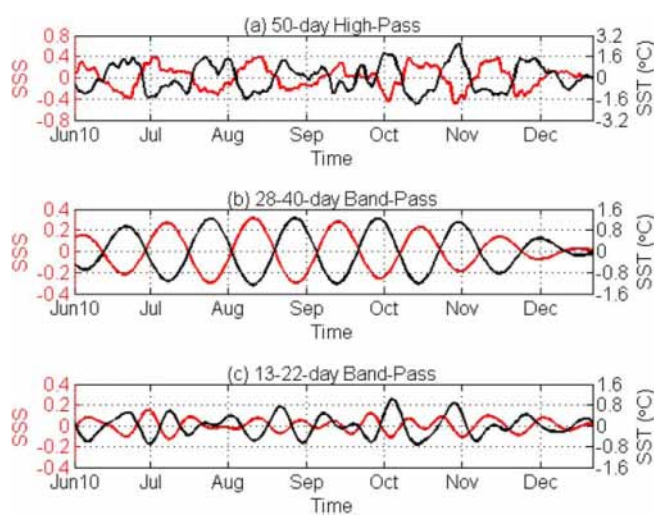


Figure 6. The filtered SMOS SSS signals (black) and OSTIA SST signals (red) at 120°W, 2°N for (a) 50d-HP, (b) 33 day, and (c) 17 day from June to December 2010.

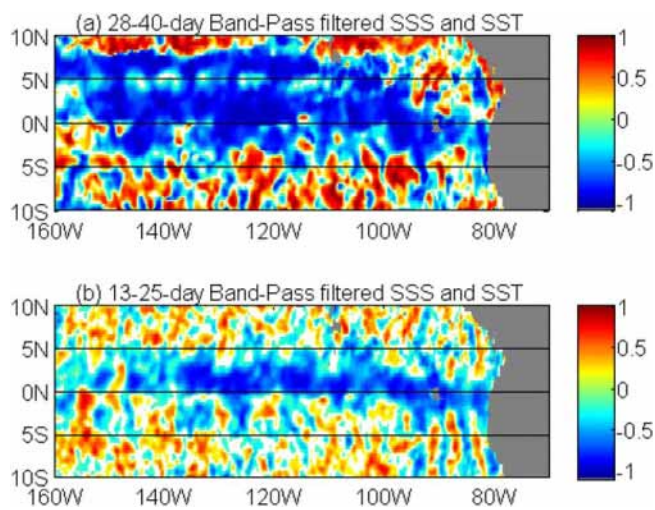


Figure 7. The correlation coefficient between filtered SSS signals and SST signals for (a) 33 day and (b) 17 day from June to December 2010. The regions where the significant level of the correlation is lower than 95% are blanked out.

ance of the fast 1.5 m/s westward 17 day propagations mostly occurs after July (Figures 8b, 8d, 9b, and 9d), at the same time as the appearance of the 33 days poleward propagation (see the latitude-time Hovmöller diagrams in Figure 10). The propagation speeds of 17 day signals reduce to 1.0 m/s at the equator from

[*Yu et al.*, 1995; *Proehl*, 1996], for which zonal velocity equals the zonal phase speed.

At the equator, both SSS and SST 17 day signals show a faster propagation that is better described by a 1.5 m/s speed (Figures 9b and 9d) which is close to the second baroclinic mode Yanai wave phase speed of \sim 1.6 m/s [*Shinoda*, 2012]. In addition, the dominant westward propagation speeds of SSS and SST 17 day signals is 0.6 m/s at 4° N, whereas they are 1.5 m/s at 2° S (not shown). This is consistent with the 17 day TIWs characteristics, which are similar to equatorially trapped Yanai wave with maximum signals between 2° S and 2° N [*Lyman et al.*, 2007; *Shinoda*, 2012]. At the equator, east of 120° W, the appear-

ance of the fast 1.5 m/s westward 17 day propagations mostly occurs after July (Figures 8b, 8d, 9b, and 9d).

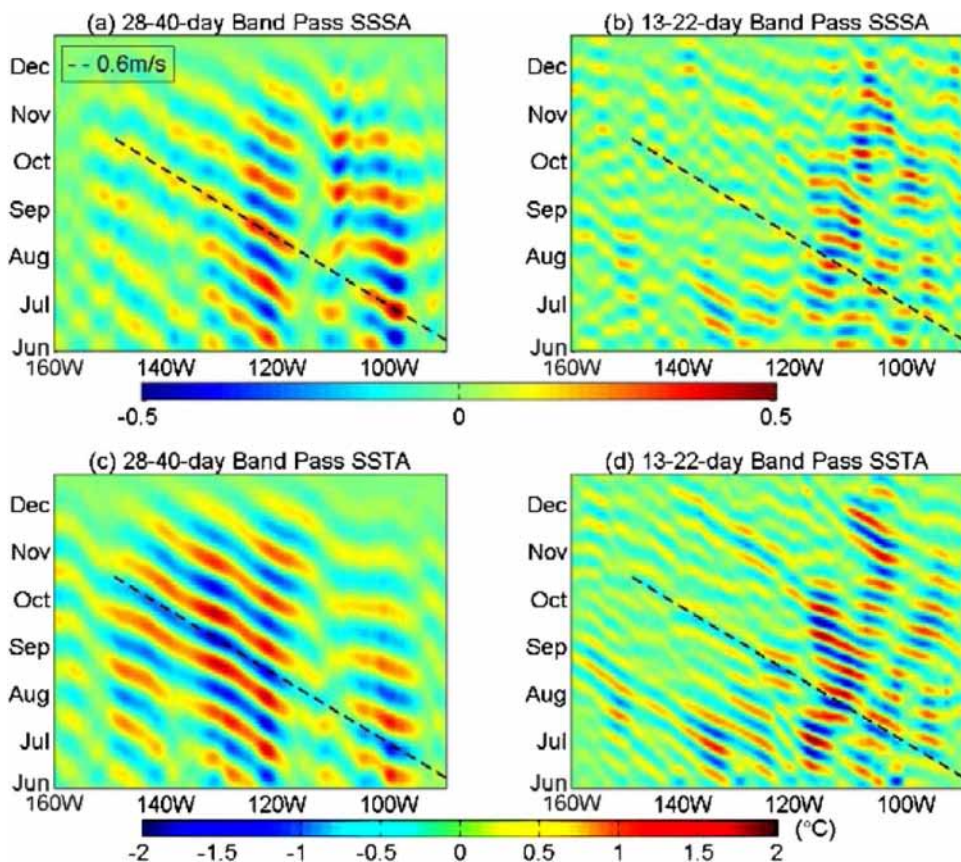


Figure 8. (a, b) Longitude-time Hovmöller diagram of the SSS and (c, d) SST signals at 2° N. The left and right columns correspond to 33 and 17 day signals, respectively. The propagation speeds of 0.6 m/s (dashed lines) are representative of the propagation speed for the 33 and 17 day signals.

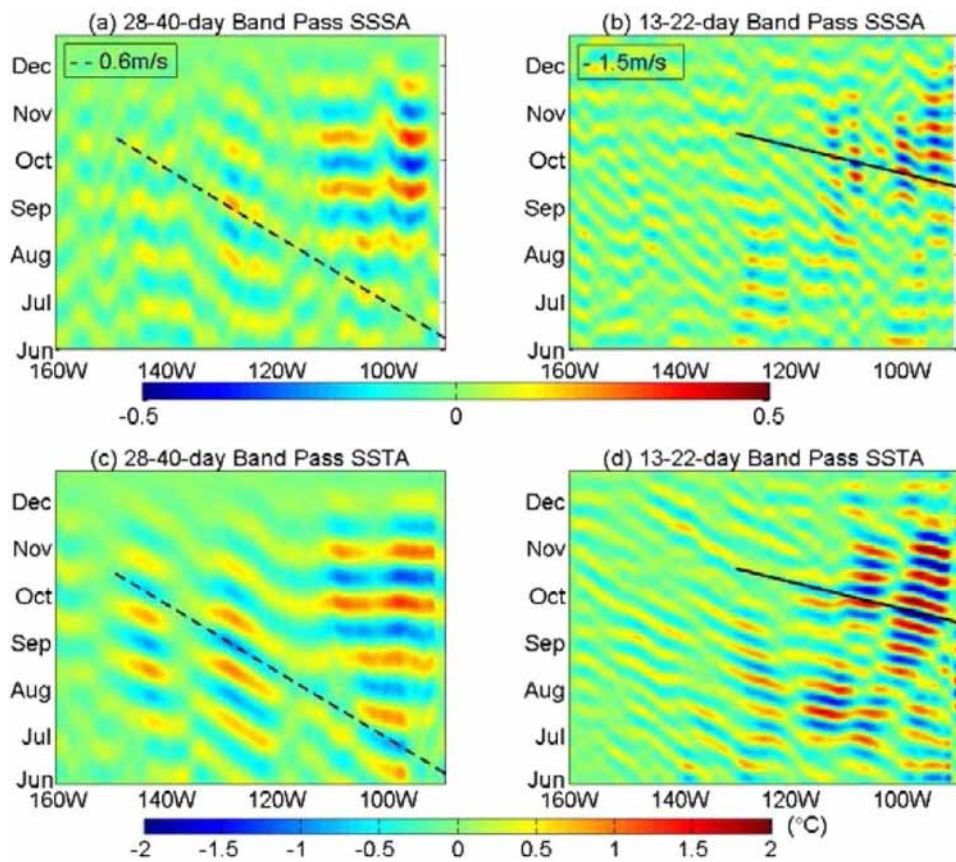


Figure 9. Same as Figure 8 except for the equator. The propagation speeds of 0.6 m/s (dashed lines) and 1.5 m/s (solid lines) are representative of the propagation speed for the 33 and 17 day signals, respectively.

September to December 2011. This period overlaps with the period of the study by *Lee et al.* [2012] who reported a 1 m/s speed of the 17 day TIWs near the equator using Aquarius data.

3.3. Seasonal Variation of TIWs

A 3 year longitude-time section in the eastern Pacific Ocean along 2°N clearly reveals westward propagations of SMOS SSS and OSTIA SST signals from 90°W to 160°W (Figure 11). The strength of these propagating signals varies seasonally and interannually. They are weaker or disappear during boreal spring (March to June period), and are much stronger during La Niña conditions, i.e., when the values of the NINO3 SST index are negative (the NINO3 region is defined in the caption of Figure 11). The 33 day SSS and SST signals appear together in time and approximately in the same regions (Figures 11c and 11f). The 17 day SSS signal is less clear than the SST counterpart (Figures 11d and 11g). The peak amplitude is ~0.5 for the SSS and 2°C for the SST. Superimposed on the seasonal variation of TIW strength are interannual variations. The amplitudes and longitudinal extents of SSS and SST signals decrease from 2010 to 2013 (Figures 11b–11g) associated with the transition from a strong La Niña to a moderate and a non-La Niña phase (see NINO3 indices in Figure 11a). The 33 day filtered SMOS SSS signals at the equator are not as strong as those at 2°N from

Table 3. The Linear Fit of Filtered SMOS SSS and OSTIA SST at [0°N–4°N, 95°W–135°W] and [0°N–4°N, 135°W–160°W] and the Correlation Coefficients r Between SMOS SSS and OSTIA SST in the Two Regions (the 95% Significant Values are Indicated in Bold Italics)

Region	33 Day Band Pass		17 Day Band Pass	
	r	Slope (1/°C)	r	Slope (1/°C)
0°N–4°N, 95°W–135°W	-0.98	-0.25	-0.77	-0.15
0°N–4°N, 135°W–160°W	-0.75	-0.12	-0.42	-0.12

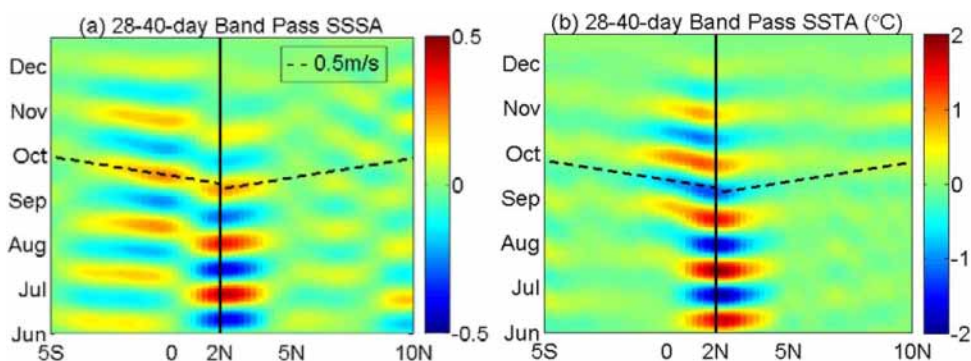


Figure 10. Latitude-time Hovmöller diagram of the 33 day (a) SSS and (b) SST signals at 100°W from June to December 2010. The poleward propagation speeds of 0.5 m/s are shown by dashed lines.

2010 to 2013 (Figures 11f and 11j). However, the 17 day filtered SMOS SSS signals are stronger at the equator than at 2°N from 2010 to 2013 (Figures 11g and 11k).

The latitude of maximum meridional gradients of SSS and hence SSS TIWs vary seasonally, with variations east of 100°W stronger than those west of 100°W (e.g., the latitude shifts between 1°N and 2°N at 120°W while the latitude shifts between 1°S and 2°N at 85°W). West of 110°W, the dominant westward propagation speed of 17 day SSS TIW at the equator is approximately 1 m/s during a moderate La Niña phase from June to December 2011 (similar to the observation by Aquarius [Lee *et al.*, 2012]) and is around 0.6 m/s during a non-La Niña phase from June to December 2012 (Figure 11k). In other words, west of 110°W, the dominant westward propagation speed of 17 day SSS TIWs in the second half of the year at the equator decreases from 1.5 to 1 m/s and to 0.6 m/s associated with the transition from a strong La Niña to moderate and non-La Niña conditions. On the contrary, the dominant westward propagation speeds of 17 day signals in the second half of the year at 2°N and 33 day signals at both the equator and 2°N west of 110°W remain very similar from 2010 to 2013 (Figures 11f, 11g, and 11j).

We then compared the 33 and 17 day SSS signals in SMOS and Aquarius at 2°N. They appear simultaneously in the same regions from September 2011 to June 2013, except that the peak amplitudes of Aquarius SSS signals (Figures 11h and 11i) are weaker than those of SMOS SSS (Figures 11f and 11g). This is likely due to lower spatial resolution and less frequent temporal samplings for the Aquarius satellite than for the SMOS satellite and the related spatial and temporal averaging during the generation of the level 3 maps.

4. Discussion and Conclusion

The SMOS retrieval scheme uses first guess geophysical parameters. If the first guess, i.e., SST or wind speed (WS) is biased, this can introduce biases on retrieved SSS [Yin *et al.*, 2014]. We have evaluated these possible biases in Appendix A and show that they do not change significantly the SSS filtered signals shown in Table 1 and Figure 11.

The variations of filtered SMOS SSS follow those of TAO SSS with high correlation coefficients and close peak amplitudes at six locations where strong TIW signals are observed in the TAO SSS. The linear fits of the SMOS SSS and the OSTIA SST filtered signals are close to the corresponding fits of TAO SSS and SST filtered signals, i.e., around $-0.20^{\circ}\text{C}^{-1}$ for the 17 day signals and around $-0.25^{\circ}\text{C}^{-1}$ for the 33 day signals. Nevertheless, differences between satellite estimates of SSS in the top centimeter of the ocean and TAO SSS at 1 m depth may be partly due to vertical dynamics of the upper-ocean, air-sea flux, and data sampling.

From June to December 2010, the tropical Pacific was characterized by a strong La Niña. Together with OSTIA SST, the SMOS SSS provides a clear view of the 2-D longitude-latitude TIW structure of SSS, SST, and their relations in the eastern tropical Pacific Ocean for the first time from space. The largest SMOS SSS and OSTIA SST TIW signals appear at around 2°N west of 110°W. They shift southward and cross the equator at 90°W following the northern SSS and SST meridional gradients all the way to the eastern boundary. An equatorially trapped band of negative correlations appears just north of the equator west of 100°W and

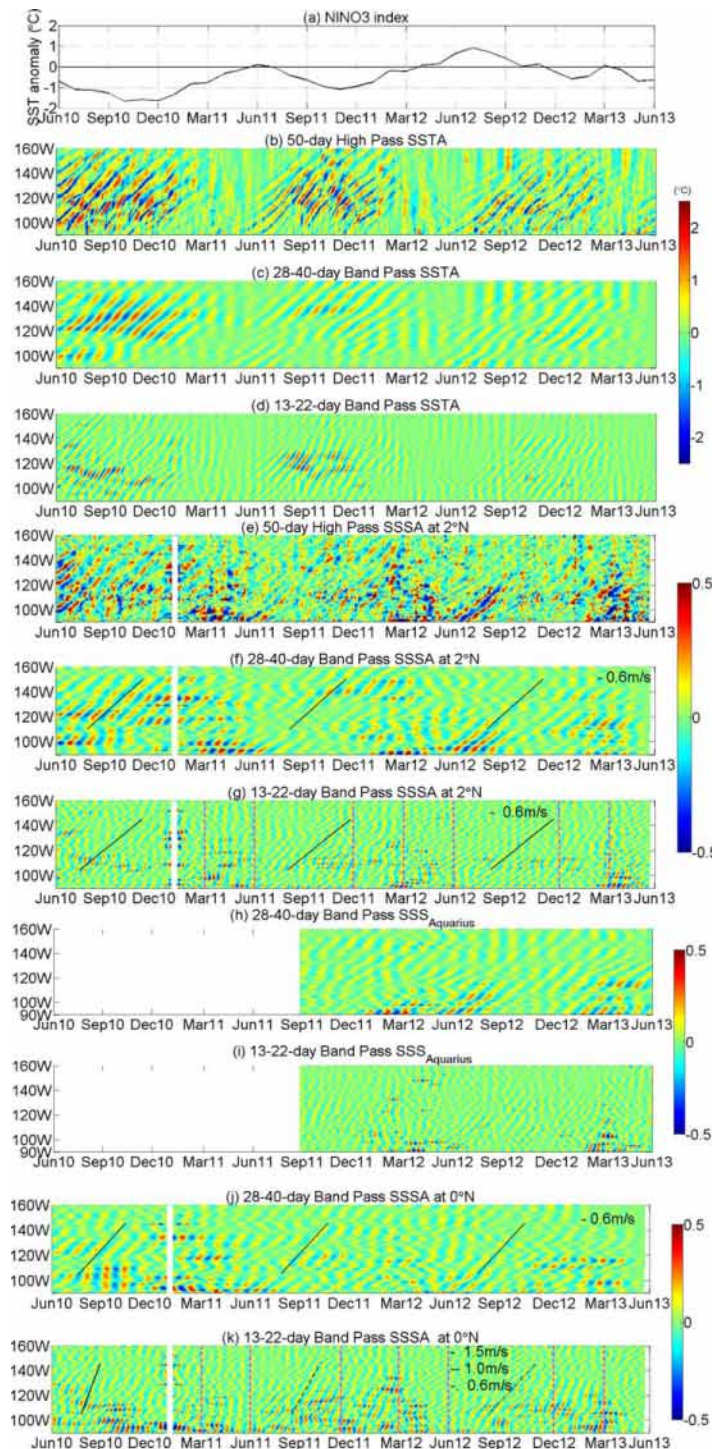


Figure 11. (a) Time series of SST anomalies in the NINO3 region (5°N – 5°S and 90°W – 150°W) from <http://www.cpc.ncep.noaa.gov/data/indices/sstoi.indices> in 2010–2013, longitude-time Hovmöller diagram of (b–d) OSTIA SST, (e–g) SMOS SSS, and (h, i) Aquarius SSS signals at 2°N , and (j, k) SMOS SSS signals at the equator. Figures 11b and 11e correspond to 50d-HP signals. Figures 11c, 11f, 11h, and 11j correspond to 33 day signals, whereas Figures 11d, 11g, 11i, and 11k correspond to 17 day signals. The SMOS SSS from 27 December 2010 to 11 January 2011 is missing due to instrumental failure of SMOS (blanks in Figures 11e–11g and 11j). The propagation speeds indicate by different types of lines in Figures 11f, 11g, 11j, and 11k. The vertical purple dash lines in Figures 11g and 11k correspond to 1 March, 1 June, and 1 December.

moves southward further east to cross the equator at 90°W , following the SSS and SST meridional gradients to the eastern boundary. In addition to the equatorial large correlation band, a band of negative correlations also exists around 8°N west of 110°W for the 33 day signals. Those signatures are related to TIWs and TIVs.

From June to December 2010, the westward propagation speed of SSS is between 0.6 and 1.5 m/s depending on latitude and dominant period of TIWs. The westward propagation speeds of SSS and SST 33 day signals at 2°N east of 110°W tend to accelerate after July 2010 and turn into latitudinal propagation after late August with meridional phase speeds of 0.5 m/s (Figures 8a, 8c, and 10). Acceleration of the westward propagation speeds and the propagation direction of 33 day signals changing in time from westward to poleward appeared also at the equator. Chelton *et al.* [2000] also noticed faster westward propagation signals in satellite microwave SST observations of TIWs in some seasons. The poleward propagation signals with opposite phase in SSS and SST extend further south than north in latitude, though they start around 2°N (Figure 10). These poleward propagation signals have similar meridional wave number and propagation speeds of 0.5 m/s (as indicated by the dashed lines in Figure 10). This speed value is similar to the zonal westward one in 33 day propagating TIWs. We did not find poleward propagation signals in the 33 day filtered altimeter sea surface height signals (www.aviso.altimetry.fr) and OSCAR current signals for the

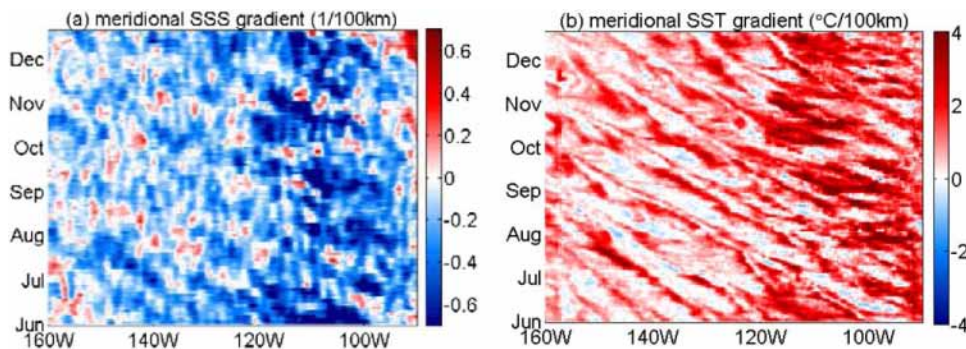


Figure 12. Longitude-time Hovmöller diagram of meridional gradients of (a) SSS and (b) SST at 2°N from June to December 2010.

same period. There is no evidence for the change in westward speed or poleward propagation in the 17 day signals. The poleward propagation is rarely mentioned by previous studies.

The east-west contrasts (with a boundary at 135°W around 2°N) of the peak amplitudes in filtered SMOS SSS signals are stronger than those in filtered OSTIA SST signals from June to December 2010. One possible reason is that the OSTIA SST meridional gradient remains positive east and west of 135°W while the negative SMOS SSS meridional gradient sometimes changes to positive value, which weakens the amplitude of SMOS SSS filtered signals toward the west (Figure 12).

The TIW signals in the SMOS SSS from June 2010 to May 2013 have approximate peak amplitudes of 0.5. Westward propagations of SMOS SSS and OSTIA SST signals appear west of 90°W seasonally and the intensity of the waves is much stronger during La Niña conditions than during non-La Niña conditions. The amplitudes and extents of SSS and SST signals decrease year by year from 2010 to 2013. West of 110°W, the dominant westward propagation speed of 17 day SSS TIWs in the second half of the year at the equator decreases from 1.5 to 0.6 m/s associated with the transition from a strong La Niña to non-La Niña conditions. Our study suggests that the 1 m/s dominant speed of the TIWs near the equator reported by *Lee et al.* [2012] was specifically associated with a moderate La Niña condition during the period of that study. On the other hand, the dominant westward propagation speed in the second half of the year does not change for the 17 day signals at 2°N and 33 day signals at both the equator and 2°N west of 110°W. From 2010 to 2013, the 33 day SMOS SSS signals are stronger at 2°N than at the equator; on the contrary, the 17 day signals remain stronger at the equator than at 2°N. There are several possible reasons for the decrease in the westward propagation speed of 17 day SSS TIWs at the equator. The phase speed of the growing wave is much larger than the decaying wave [*Jochum et al.*, 2004]. It also suggests that higher TIW speeds are for periods of stronger upwelling [*Caltabiano et al.*, 2005] and of the more intense South Equatorial Current [*Masina and Philander*, 1999]. In addition, the change in the phase speed depends on the properties of the most unstable barotropic or baroclinic processes [*Jochum et al.*, 2004].

The SMOS satellite mission provide an unprecedented and successful space-borne observation of the SSS from 2010 to 2013 allowing the study of the SSS variations associated with TIWs during strong, moderate, and non-La Niña years. The synoptic coverage of SMOS SSS complements in situ salinity observations by ARGO floats and TAO moorings in resolving TIWs and TIVs. The results presented here facilitate studies of TIWs using space-based SMOS SSS and provide confidence in using SMOS SSS to constrain models and to assimilate SMOS SSS into models.

Appendix A: Possible Artificial Signals of SSS Anomaly in the SMOS Retrieval

The objective of this appendix is to quantify the possible erroneous SSS signals in the SMOS retrieval process.

The SST used in the SMOS SSS retrievals is taken from European Centre for Medium-range Weather Forecasts (ECMWF) Meteorological Archival and Retrieval System (MARS) archive which uses OSTIA SST.

Although there are noticeable differences between the OSTIA SST and the SST from daily AVHRR-based Optimal Interpolation Sea Surface Temperature [*Reynolds et al.*, 2007], the SSS filtered signals shown in Figure 11 are not artificial signatures in the SMOS SSS retrievals due to discrepancies between the two SST.

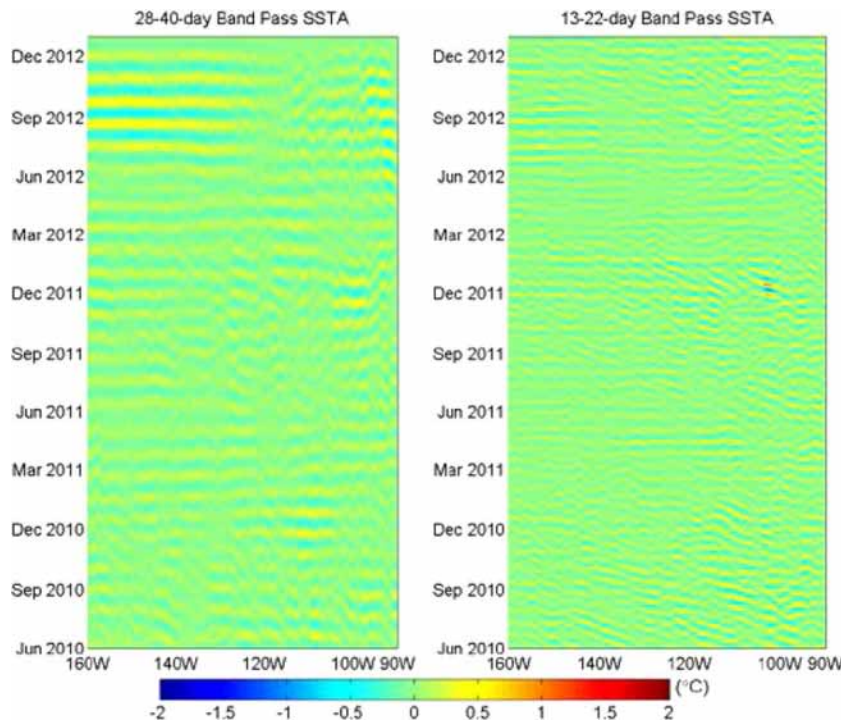


Figure A1. Longitude-time Hovmöller diagram of filtered signals of differences between the OSTIA and the Reynolds SST at 2°N . The left and right columns correspond to 33 and 17 day signals.

We compare the SMOS SSS currently retrieved using OSTIA SST with the ones that would have been retrieved using the Reynolds SST product (<http://www.ncdc.noaa.gov/sst/>) that is used in the Aquarius retrieval. The 33 day signals of differences between OSTIA and Reynolds SST at 2°N are $<0.5^{\circ}\text{C}$ in

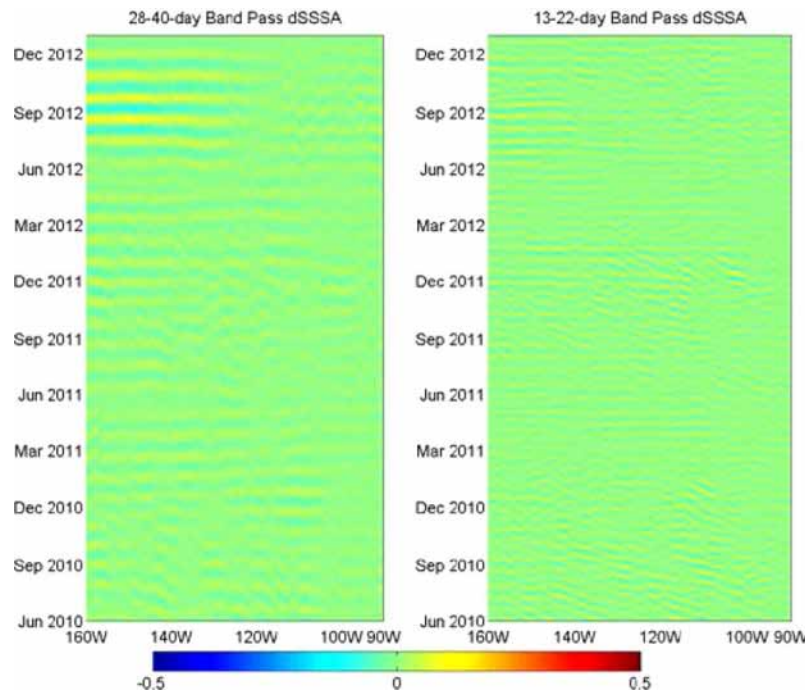


Figure A2. Same as A1 except for the estimated SSS differences due to differences between OSTIA and Reynolds SST in the retrievals using the dielectric model [Klein and Swift, 1977] implemented in the ESA L2OS processor.

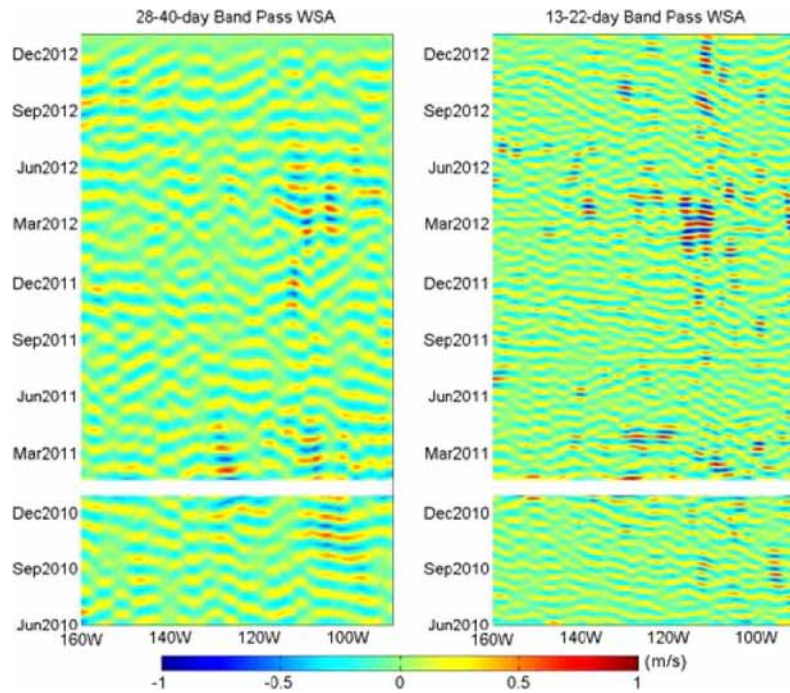


Figure A3. Same as A1 except for differences between SMOS retrieved WS and SSMIS WS. The SMOS SSS from 27 December 2010 to 11 January 2011 is missing due to instrumental failure of SMOS (blanks).

magnitude (Figure A1, left). SSS differences due to differences between OSTIA and Reynolds SST in the retrievals are estimated using the dielectric model [Klein and Swift, 1977] implemented in the ESA level 2 ocean salinity (L2OS) processor. The 33 day signals of estimated SSS differences due to differences in SST

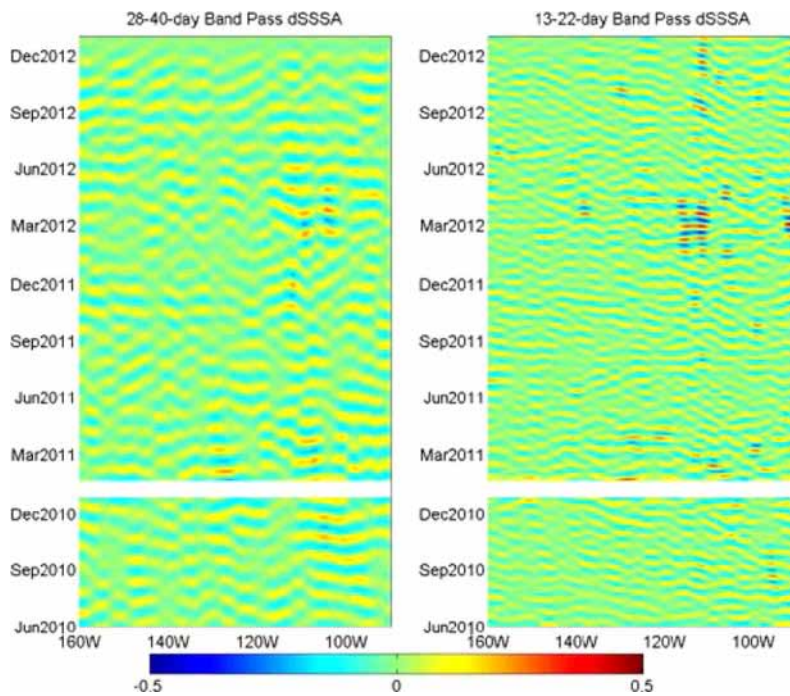


Figure A4. Same as A1 except for the estimated SSS differences due to differences between SMOS retrieved WS and SSMIS WS in the retrievals using the roughness model [Yin et al., 2012b] implemented in the ESA L2OS processor. The SMOS SSS from 27 December 2010 to 11 January 2011 is missing due to instrumental failure of SMOS (blanks).

are <0.03 in magnitude (Figure A2, left), which is much less than what is observed in SMOS SSS (Table 1). The 17 day signals of differences between the OSTIA and the Reynolds SST at 2°N are $<1^{\circ}\text{C}$ in magnitude (Figure A1, right). The 17 day signals of estimated SSS differences due to differences in SST are <0.05 in magnitude (Figure A2, right), which is also much less than what is observed in SMOS SSS (Table 1).

The wind speed (WS) provided by the ECMWF is used as the first guess to initialize the retrieval process of SMOS SSS in order to correct for surface roughness effect on brightness temperature (TB). There are systematic inconsistencies between the atmospheric WS modeled using ECMWF and the WS sensed by radiometers like the Special Sensor Microwave Imager/Sounder (SSMIS). The inconsistencies of WS are reduced by the SMOS retrieval scheme but they still lead to residual biases in the SMOS SSS [Yin et al., 2014]. However, there is no evidence of westward propagations in the estimated SSS differences due to differences in WS. The differences in 33 day signals between the SMOS retrieved WS and the SSMIS WS at 2°N are <0.5 m/s in magnitude (Figure A3, left). SSS differences due to differences between SMOS retrieved WS and SSMIS WS in the retrievals are estimated using the roughness model [Yin et al., 2012b] implemented in the ESA L2OS processor. The differences in 33 day SSS due to differences in WS are <0.2 in magnitude (Figure A4, left). The 17 day differences between the SMOS retrieved WS and the SSMIS WS at 2°N are <1 m/s in magnitude (Figure A3, right). The differences in 17 day SSS due to differences in WS are <0.4 (Figure A4, right). However, there is no evidence of westward propagation in the estimated SSS differences due to differences in WS, which is different from the westward signals observed by SMOS SSS.

Acknowledgments

We thank two anonymous reviewers for their constructive comments. This work was funded by the European Space Agency (ESA) Support to Science element project entitled SMOS + Surface Ocean and Synergy and by the CNES/TOSCA/SMOS-GOSCAL project. Daily SSS from LOCEAN is available upon request submitted to J. Boutin and the CATDS CEC-IFREMER SSS is obtained from the Ocean Salinity Expertise Center (CECOS) of the CNES-IFREMER Centre Aval de Traitement des Données SMOS (<http://www.catds.fr/Products/Available-products-from-CEC-OS/Ifremer-Dataset-V02>). The authors would like to acknowledge the Met office for providing OSTIA SST (http://ghrsst-pp.metoffice.com/pages/latest_analysis/ostia.html), the National Climatic Data Center (NCDC) for providing Reynolds SST (<http://www.ncdc.noaa.gov/sst>), and the TAO Project Office/Pacific Marine Environmental Laboratory for providing TAO SSS and SST (<http://www.pmel.noaa.gov/tao>). The Aquarius Combined Active Passive (CAP) algorithm level 3 Sea Surface Salinity was obtained from the Physical Oceanography Distributed Active Archive Center (PO.DAAC) at the NASA Jet Propulsion Laboratory, Pasadena, CA (http://podaac.jpl.nasa.gov/dataset/AQUARIUS_L3_SSS_CAP_7DAY_V2). The authors would like to acknowledge the OSCAR Project Office for providing current data (<http://www.oscar.noaa.gov>).

References

- Bonjean, F., and G. S. E. Lagerloef (2002), Diagnostic model and analysis of the surface currents in the tropical Pacific Ocean, *J. Phys. Oceanogr.*, **32**, 2938–2954, doi:10.1175/1520-0485(2002)032<2938:DMAOT>2.0.CO;2.
- Boutin, J., et al. (1999), Satellite sea surface temperature: A powerful tool for interpreting in situ pCO₂ measurements in the equatorial Pacific Ocean, *Tellus, Ser. B*, **51**(2), 490–508.
- Boutin, J., N. Martin, G. Reverdin, X. Yin, and F. Gaillard (2013), Sea surface freshening inferred from SMOS and ARGO salinity: Impact of rain, *Ocean Sci.*, **9**, 183–192, doi:10.5194/os-9-183-2013.
- Caltabiano, A., I. Robinson, and L. Pezzi (2005), Multi-year satellite observations of instability waves in the Tropical Atlantic Ocean, *Ocean Sci.*, **1**, 97–112.
- Challenor, P., P. Cipollini, and D. Cromwell (2001), Use of the 3D radon transform to examine the properties of Oceanic Rossby waves, *J. Atmos. Oceanic Technol.*, **18**(9), 1558–1566.
- Chelton, D. B., F. J. Wentz, C. L. Gentemann, R. A. de Szoeke, and M. G. Schlax (2000), Satellite microwave SST observations of transequatorial tropical instability waves, *Geophys. Res. Lett.*, **27**, 1239–1242, doi:10.1029/1999GL011047.
- Corbella, I., F. Torres, N. Duffo, V. González-Gambau, M. Pablos, I. Duran, and M. Martín-Neira (2011), MIRAS calibration and performance: Results from the SMOS in-orbit commissioning phase, *IEEE Trans. Geosci. Remote Sens.*, **49**(9), 3147–3155.
- Dutrieux, P., C. Menkes, J. Vialard, P. Flament, and B. Blanke (2008), Lagrangian study of tropical instability vortices in the Atlantic, *J. Phys. Oceanogr.*, **38**, 400–417, doi:10.1175/2007JPO3763.1.
- Donlon, C. J., M. Martin, J. D. Stark, J. Roberts-Jones, E. Fiedler, and W. Wimmer (2012), The operational sea surface temperature and sea ice analysis (OSTIA), *Remote Sens. Environ.*, **116**, 140–158, doi:10.1016/j.rse.2010.10.017.
- Evans, W., P. G. Strutton, and F. P. Chavez (2009), Impact of tropical instability waves on nutrient and chlorophyll distributions in the equatorial Pacific, *Deep Sea Res., Part I*, **56**, 178–188, doi:10.1016/j.dsr.2008.08.008.
- Gorgues, T., C. Menkes, O. Aumont, J. Vialard, Y. Dandonneau, and L. Bopp (2005), Biogeochemical impact of tropical instability waves in the equatorial Pacific, *Geophys. Res. Lett.*, **32**, L24615, doi:10.1029/2005GL024110.
- Grodsky, S. A., J. A. Carton, C. Provost, J. Servain, J. A. Lorenzetti, and M. J. McPhaden (2005), Tropical instability waves at 0°N , 23°W in the Atlantic: A case study using Pilot Research Moored Array in the Tropical Atlantic (PIRATA) mooring data, *J. Geophys. Res.*, **110**, C08010, doi:10.1029/2005JC002941.
- Henocq, C., J. Boutin, G. Reverdin, F. Petitcolin, S. Arnault, and P. Lattes (2010), Vertical variability of near-surface salinity in the tropics: Consequences for L-band radiometer calibration and validation, *J. Atmos. Oceanic Technol.*, **27**, 192–209.
- Jochum, M., and R. Murtugudde (2006), Temperature advection by tropical instability waves, *J. Clim.*, **36**, 592–605.
- Jochum, M., P. Malanotte-Rizzoli, and A. Busalacchi (2004), Tropical instability waves in the Atlantic Ocean, *Ocean Modell.*, **7**, 145–163.
- Kennan, S. C., and P. J. Flament (2000), Observations of a tropical instability vortex, *J. Phys. Oceanogr.*, **30**, 2277–2301, doi:10.1175/1520-0485(2000)030<2277:OOTAIV>2.0.CO;2.
- Klein, L., and C. Swift (1977), An improved model for the dielectric constant of sea water at microwave frequencies, *IEEE Trans. Antennas Propag.*, **AP-25**(1), 104–111.
- Lagerloef, G., et al. (2008), The Aquarius/SAC-D mission—Designed to meet the salinity remote sensing challenge, *Oceanography*, **21**(1), 68–81, doi:10.5670/oceanog.2008.68.
- Lee, T., G. Lagerloef, M. G. Gierach, H.-Y. Kao, S. Yueh, and K. Dohan (2012), Aquarius reveals salinity structure of tropical instability waves, *Geophys. Res. Lett.*, **39**, L12610, doi:10.1029/2012GL052232.
- Legeckis, R. V., and G. Reverdin (1987), Long waves in the equatorial Atlantic Ocean during 1983, *J. Geophys. Res.*, **92**, 2835–2842, doi:10.1029/JC092iC03p02835.
- Liu, T. W., X. Xie, P. S. Polito, S. Xie, and H. Hashizume (2000), Atmospheric manifestation of tropical instability wave observed by QuikSCAT and tropical rain measuring mission, *Geophys. Res. Lett.*, **27**, 2545–2548, doi:10.1029/2000GL011545.
- Lyman, J. M., G. C. Johnson, and W. S. Kessler (2007), Distinct 17- and 33-day tropical instability waves in subsurface observations, *J. Phys. Oceanogr.*, **37**, 855–872, doi:10.1175/JPO3023.1.

- Masina, S., and S. G. H. Philander (1999), An analysis of tropical instability waves in a numerical model of the Pacific Ocean: 1. Spatial variability of the waves, *J. Geophys. Res.*, 104, 29,613–29,635, doi:10.1029/1999JC900227.
- Masina, S., S. G. H. Philander, and A. B. G. Bush (1999), An analysis of tropical instability waves in a numerical model of the Pacific Ocean: 2. Generation and energetics of the waves, *J. Geophys. Res.*, 104, 29,637–29,661, doi:10.1029/1999JC900226.
- McClain, C., J. Christian, S. Signorini, M. Lewis, I. Asanuma, D. Turk, and C. Dupouy-Douchement (2002), Satellite ocean-color observations of the tropical Pacific Ocean, *Deep Sea Res., Part II*, 49, 2533–2560, doi:10.1016/S0967-0645(02)00047-4.
- Menkes, C., et al. (2002), A whirling ecosystem in the equatorial Atlantic, *Geophys. Res. Lett.*, 29(11), doi:10.1029/2001GL014576.
- Menkes, C., J. Vialard, S. Kennan, J. Boulanger, and G. Madec (2006), A modeling study of the impact of tropical instability waves on the heat budget of the eastern equatorial Pacific, *J. Phys. Oceanogr.*, 36, 847–865, doi:10.1175/JPO2904.1.
- Polito, P. S., J. P. Ryan, W. T. Liu, and F. P. Chavez (2001), Oceanic and atmospheric anomalies of tropical instability waves, *Geophys. Res. Lett.*, 28, 2233–2236, doi:10.1029/2000GL012400.
- Proehl, J. A. (1996), Linear stability of equatorial zonal flows, *J. Phys. Oceanogr.*, 26(4), 601–621.
- Qiao, L., and R. H. Weisberg (1995), Tropical instability wave kinematics: Observations from the tropical instability wave experiment, *J. Geophys. Res.*, 100, 8677–8693, doi:10.1029/95JC00305.
- Reul, N., and J. Tenerelli (2011), SMOS level 3 SSS research products—Product validation document—Reprocessed year 2010, *Tech. Doc. No. CATDS-CECOS-L3-VALDOC, 1(0)*, IFREMER/CNES, Plouzané, France. [Available at www.catds.fr.]
- Reynolds, R. W., T. Smith, C. Liu, D. Chelton, K. Casey, and M. G. Schlax (2007), Daily high-resolution blended analyses for sea surface temperature, *J. Clim.*, 20, 5473–5496, doi:10.1175/2007JCLI1824.1.
- Shinoda, T. (2012), Observation of first and second baroclinic mode Yanai waves in the ocean, *Q. J. R. Meteorol. Soc.*, 138, 1018–1024.
- Shinoda, T., G. N. Kiladis, and P. E. Roundy (2009), Statistical representation of equatorial waves and tropical instability waves in the Pacific Ocean, *Atmos. Res.*, 94(1), 37–44, doi:10.1016/j.atmosres.2008.06.002.
- Strutton, P. G., J. P. Ryan, and F. P. Chavez (2001), Enhanced chlorophyll associated with tropical instability waves in the equatorial Pacific, *Geophys. Res. Lett.*, 28, 2005–2008, doi:10.1029/2000GL012166.
- Swenson, M. S., and D. V. Hansen (1999), Tropical Pacific Ocean mixed layer heat budget: The Pacific cold tongue, *J. Phys. Oceanogr.*, 29, 69–81.
- Vialard, J., C. Menkes, D. L. T. Anderson, and M. A. Balmaseda (2003), Sensitivity of Pacific Ocean tropical instability waves to initial conditions, *J. Phys. Oceanogr.*, 33, 105–121.
- Willett, C., R. Leben, and M. F. Lavin (2006), Eddies and tropical instability waves in the eastern tropical Pacific: A review, *Prog. Oceanogr.*, 69(2–4), 218–238.
- Yin, X., J. Boutin, and P. Spurgeon (2012a), First assessment of SMOS data over open ocean: Part I Pacific Ocean, *IEEE Trans. Geosci. Remote Sens.*, 50(5), 1648–1661.
- Yin, X., J. Boutin, N. Martin, and P. Spurgeon (2012b), Optimization of L-band sea surface emissivity models deduced from SMOS data, *IEEE Trans. Geosci. Remote Sens.*, 50(5), 1414–1426.
- Yin, X., J. Boutin, N. Martin, P. Spurgeon, J. Vergely, and F. Gaillard (2014), Errors in SMOS sea surface salinity and their dependency on a priori wind speed, *Remote Sens. Environ.*, 146, 159–171, doi:10.1016/j.rse.2013.09.008.
- Yu, J., and W. T. Liu (2003), Seasonal and interannual variations of northern and southern tropical instability waves and their coupling with the atmosphere, *Geophys. Res. Lett.*, 30(14), 1735, doi:10.1029/2003GL017176.
- Yu, Z., J. McCreary, and J. Proehl (1995), Meridional asymmetry and energetics of tropical instability waves, *J. Phys. Oceanogr.*, 25(12), 2997–3007.
- Yueh, S., W. Tang, A. Fore, G. Neumann, A. Hayashi, A. Freedman, J. Chaubell, and G. Lagerloef (2013), L-band passive and active microwave geophysical model functions of ocean surface winds and applications to Aquarius retrieval, *IEEE Trans. Geosci. Remote Sens.*, 51(9), 4619–4632.